Simulation of Turbulent Precipitation in a Semi-batch Taylor-Couette Reactor Using CFD

D. L. Marchisio and A. A. Barresi
Dip. Scienza dei Materiali ed Ingegneria Chimica, Politecnico di Torino, 10129, Torino, Italy

R. O. Fox
Dept. of Chemical Engineering, Iowa State University, Ames, IA 50011

A finite-mode probability density function method was used with a computational fluid dynamics code to model the semibatch precipitation of barium sulfate from aqueous solutions of barium chloride and sodium sulfate in a Taylor-Couette reactor. It was simulated in turbulent flow at high Taylor numbers under the assumption of axial symmetry. The flow field was modeled using two different turbulence models, and flow predictions were validated using experimental tracer dispersion measurements. The crystal-size distribution (CSD) was calculated in terms of the first five moments considering both nucleation and growth, while neglecting the effect of aggregation. The effect of the operating conditions on the CSD was studied, and code predictions were compared with experimental data.

Introduction

Precipitation of sparingly soluble salts is an important process in the production of several materials such as catalysts, proteins, pharmaceutical products, pigments, and silver halide for the photographic industry. The final product quality of the materials obtained by this unit operation is strongly influenced by crystal morphology and CSD. The process involves three different steps: chemical reaction, nucleation, and growth. Since the first two steps are very fast, the process is defined "mixing sensitive," in the sense that the rate is not controlled by precipitation kinetics only, but also by mixing.

Several authors have studied the role of mixing in precipitation using different reactors under continuous and semi-batch conditions. Fitchett and Tarbell (1990) working with a double-feed MSMPR studied the effect of several parameters on the reactor performance. Pohorecky and Baldyga (1985, 1988) and Baldyga et al. (1990) investigated the effect of initial concentration of the reactants, feed time, and stirrer speed on the solid characteristics in a semi-batch reactor. Kim and Tarbell (1996), studying the effect of the operating conditions on the final CSD in a MSMPR, found controversial results for the effect of the stirrer speed. Baldyga et al. (1995) reviewed the available data and found that whereas it is clear that mixing controls the generation of supersaturation and thus the final CSD, it is impossible to predict intuitively the effect that the operating conditions have on the solid characteristics. For this reason, a modeling approach provides a useful tool for reactor performance prediction, design, and scale-up.

Several mechanistic models have been used, such as the Engulfment and the EDD model or the Environments model (Pohorecky and Baldyga, 1985; Garside and Tavare, 1985; Baldyga et al., 1995). In recent years, CFD has been successfully applied to model mixing-controlled problems, such as precipitation, and has also been used to predict the resulting CSD of the dispersed phase. Pipino et al. (1995) using a full probability density function (PDF) method and a CFD code for the flow field prediction, studied instantaneous nucleation, but they did not follow crystal growth. On the other hand, Wei and Garside (1997) used a CFD code to model a precipitation reactor, but they did not include a micromixing model, completely neglecting the role of mixing at the molecular level. Baldyga and Orciuch (1997, 1999) discussed the effect of mixing in a tubular reactor using a presumed-beta PDF coupled with CFD, and Piton et al. (2000) compared these results with the prediction obtained using a finite-mode PDF model.

Correspondence concerning this article should be addressed to D. L. Marchisio.

In this work, barium sulfate precipitation in a semi-batch Taylor-Couette reactor has been modeled with a finite-mode PDF model coupled with a CFD code (FLUENT). The Taylor-Couette reactor has been shown to be particularly interesting for the control of the turbulence for the ability to provide different fluid dynamic regimes, and to create turbulence without a blade type mixer, which may cause breakage of the crystals (Barresi et al., 1999). The model predictions have been validated with experimental data from the Taylor-Couette reactor. The CSD has been measured with a Coulter LS 230 laser granulometer, and the solid concentration has been calculated by measuring the residual reactant concentrations using a conductimetric technique.

Experimental Setup

Taylor-Couette reactor

The Taylor-Couette reactor is made of two coaxial cylinders with the inner one rotating. The fluid is contained in the gap between the two cylinders, and different fluid dynamic regimes are achieved depending on the rotational speed of the inner cylinder. A measure of the state of the flow is represented by the dimensionless Taylor and Reynolds numbers, which are defined by the following equations

$$Ta = \frac{\Omega_1^2 r_1 d^3}{\nu^2} \tag{1}$$

$$Re = \frac{\Omega_1 r_1 d}{\nu} \tag{2}$$

where Ω_1 is the speed of the inner cylinder, r_1 is the radius of the inner cylinder, d is the annular gap between the two cylinders, and ν is the kinematic viscosity. In his pioneering work, Taylor (1923) describes the transition between a laminar flow, known as the Couette flow, and a flow with toroidal vortices, known as the Taylor vortex flow. This transition occurs when the Taylor (or Reynolds) number exceeds a critical value. A further increase in the Taylor number causes a change in the shape of the vortices and at high values a fully turbulent flow without vortices is achieved. Smith and Townsend (1982) estimated this transition at a Taylor number 10^5 times higher than the Taylor number of the first transition.

The Taylor-Couette reactor used in this work has an inner radius (r_1) equal to 0.041 m whereas the annular gap (d) is 0.014 m. The reactor is 0.205 m high and the critical Taylor number is 1984. The reactor is shown in Figure 1. The rotational speed of the inner cylinder has been varied between 100 and 1,000 rpm, and, consequentially, the Taylor number varies between 1.2×10^7 and 1.2×10^9. These values give a Taylor number ratio very close to 10^5, and thus the reactor operates in the region between turbulent vortex flow and fully turbulent flow. In the CFD modeling, the presence of the injection tube is assumed to have negligible influence on the flow field. During the injection period, fluid is removed from the top of the reactor so that the reaction volume remains constant. Since the injection volume is small compared to the total volume of the reactor, the system behaves nearly as a semi-batch reactor during the injection period.

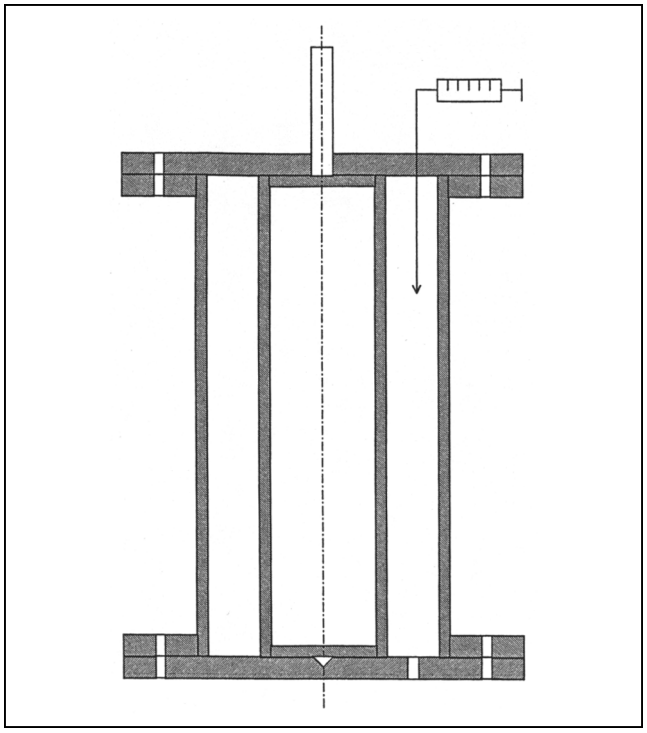

Figure 1. Axial section of the Taylor-Couette cell.

Experimental investigation of macromixing

In order to collect information about macromixing and the flow field in the reactor, a set of nonreactive tracer dispersion experiments have been carried out. The reactor was first filled with microfiltered water, and a solution of potassium chloride was then injected in the main flow direction using a small tube (outer diameter 2 mm, inner diameter 1 mm) located 70 mm from the top of the reactor in the middle of the annular gap (see Figure 1). Note that the injection point is nearer to the top of the reactor so that poor macromixing will result in a higher concentration in the top of the reactor than would be observed in a perfectly mixed reactor.

During the injection, samples of the outlet flow from a purge at the top of the reactor were collected, and the concentration of the tracer was measured using a conductimetric technique. The effects of the rotational speed of the inner cylinder and the injection velocity on macromixing were investigated. The results show that mixing in the azimuthal direction is very fast, and that when the rotational speed of the inner cylinder is increased or the injection velocity is reduced, the tracer concentration in the reactor is more uniform. Consequently, in this respect the reactor is similar to a perfectly mixed reactor.

In fact, by plotting the outlet dimensionless tracer concentration (moles leaving the reactor normalized by the total number of moles introduced n/n_0) against the dimensionless injected volume (ratio between the injected volume and the reactor volume V_i/V_r), a decrease in the slope of the profiles (more uniform mixing) is obtained with increasing rotational speed of the inner cylinder or with decreasing injection velocity (see experimental data in Figure 2 or Figure 3). These results confirm what has been found in previous work

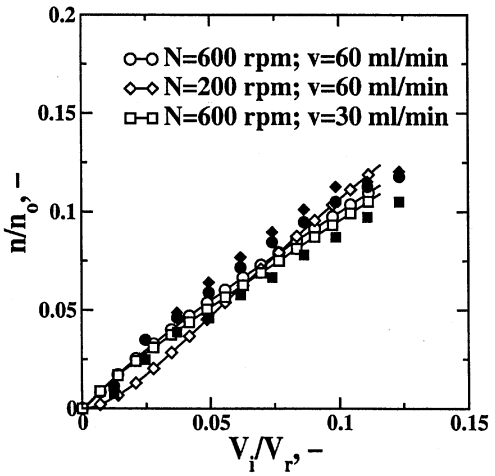

Figure 2. CFD predictions with the RNG k-ϵ model (open symbols) vs. experimental data (filled symbols) under different operating conditions.

(Marchisio et al., 1998) in a continuous Taylor-Couette reactor. Moreover, comparison with a perfectly mixed reactor with the same injection velocities showed that results in this limiting case were always below the experimental curves.

Experimental investigation of barium sulfate precipitation

Experiments for barium sulfate precipitation from aqueous solutions of sodium sulfate and barium chloride were carried out in the Taylor-Couette reactor working in semi-batch conditions. Microfiltered water and analytical chemicals were used to prepare the solutions. The reactor was first filled with a sodium sulfate solution, and barium chloride was then added with a constant injection velocity. After 200 s, samples taken from the bottom of the reactor were analyzed. The CSD

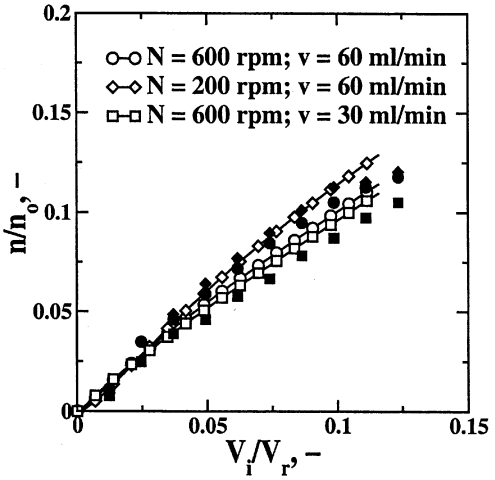

Figure 3. CFD predictions with the RSM (open symbols) vs. experimental data (filled symbols) under different operating conditions.

was determined using a laser granulometer (Coulter LS 230), whereas the solid concentration was calculated by measuring the residual reactant concentrations with a conductimetric technique.

The rotational speed of the inner cylinder was varied between 100 and 1,000 rpm, whereas the initial nominal supersaturation ($S_o = \langle c_A^0 \rangle \langle c_B^0 \rangle / k_s$) was varied between 10^4 and 10^6. This parameter is the ratio of the product of the reactant concentrations in the case of complete mixing without reaction (that is, $\langle c_A^0 \rangle$ and $\langle c_B^0 \rangle$) and the solubility product of barium sulfate (k_s).

The effect of the injection velocity was studied in the range between 30 and 100 mL/min and the volume ratio between the two solutions (f), which represents the total volume of barium chloride injected divided by the volume of sodium sulfate present in the reactor, was varied between 0.1 and 0.001. The inlet concentrations of the two reactants (c_{Ao}, c_{Bo}) and the injection time were chosen such that the overall stoichiometric ratio was always 1:1.

Flow Field Simulations

The turbulent Taylor-Couette cell has been modeled using FLUENT (v. 5.2). Because of the high swirl of the mean flow field, mixing in the azimuthal direction is very fast and the assumption of axial symmetry can be used (that is, the mean velocity $\langle \boldsymbol{u} \rangle$ depends only on r and z). Two-dimensional (2-D) simulations, on an axial plane of the reactor, have been carried out using an unstructured grid with a finer resolution near the injection point and an outflow positioned at the top of the reactor. The final grid contained 3,050 cells, 6,321 faces, and 3,281 nodes.

Two different turbulence models have been compared. The first one is the RNG k-ϵ model. In this model, two equations are added to the continuity and the Reynolds-averaged Navier-Stokes equations. These equations are derived using a statistical technique (renormalization group theory), and the method represents a refinement of the standard k-ϵ method, with enhanced accuracy, in particular for swirling flow. The second one is the Reynolds Stress Model (RSM), which is the most elaborate turbulence model available in FLUENT. In this model the isotropic eddy-viscosity hypothesis is abandoned, and four (2-D) or seven (3-D) equations are added to the Navier-Stokes/continuity equations. The added equations are the Reynolds stress transport equations and the equation for the dissipation rate. Because of the anisotropic formulation of the problem using the RSM, a more accurate flow field prediction should be obtained in swirling flow [for details on the two models, see Fluent (1998) and Valerio et al. (1998)].

Using either model, FLUENT predicts a mean flow with standing vortices and in all the runs the vortices were counter-rotating and even in number. For a rotational speed of the internal cylinder of 600 rpm and an injection velocity of 30 mL/min, eight vortices were predicted by both models. The value of the swirl velocity at the moving wall is 2.58 m/s, whereas the average value in all the volume is 0.845 m/s for the RNG k-ϵ model and 0.924 m/s for the RSM. Both the radial and axial mean velocity have a maximum value of 0.281 m/s for the RNG k-ϵ model, whereas, for the RSM, the maximum for the mean radial velocity is 0.75 m/s, and for the

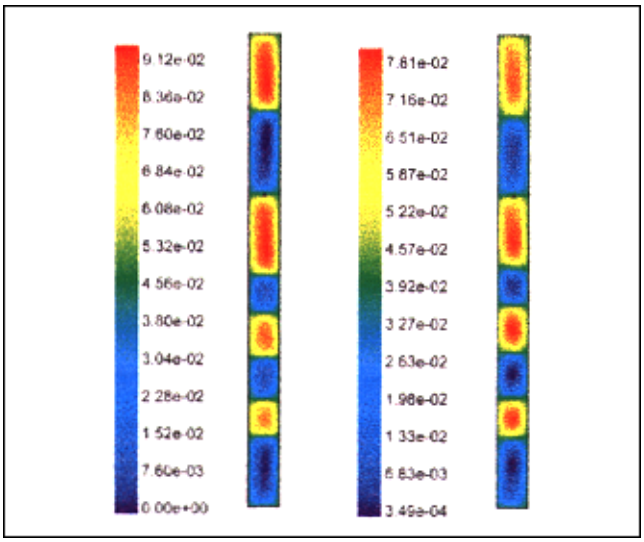

Figure 4. Stream function (kg/s) for $N = 600$ rpm and $v = 30$ mL/min with the RNG k-ϵ model (left) and the RSM (right).

mean axial velocity is 0.80 m/s. Stream function plots for this case using the two models are reported in Figure 4.

Ideally, the CFD predictions should be validated using a detailed experimental measurement of the flow field using, for example, a PIV technique. However, because these data are not available for this reactor (and difficult to obtain without extensive modifications of the experimental apparatus), the flow field predictions have been used to predict the tracer dispersion in the reactor, which can be easily measured. The simulation results obtained carrying out a set of time-dependent simulations, with a local injection of tracer in the inlet zone, have been compared with experimental data.

In Figures 2 and 3, the comparisons between experimental data and CFD predictions are reported. Although it is difficult to discriminate between the two, from the figures, it is possible to conclude that unlike the RNG k-ϵ model, the RSM gives the correct qualitative prediction of the influence of the operating conditions. In fact, using this model, the decrease of the slope profiles for increasing N or decreasing v is better reproduced by the model. Hereinafter, the RSM is used to carry out all simulations.

Precipitation Model

The description of precipitation requires a micromixing model for the liquid phase where the fast chemical reaction occurs, and a population balance for the solid phase. The first takes into account the mixing dynamics on the molecular level, whereas the second takes into account nucleation of the solid phase and growth of the crystals. Since the two models have to be coupled with FLUENT using user-defined subroutines, a simple but accurate approach is preferable.

Finite-mode PDF method

A finite-mode PDF model has been chosen to model micromixing. In this approach every cell of the computational domain contains N different modes or environments, which correspond to a discretization of the composition PDF in a finite set of delta functions (Fox, 1998)

$$f_\phi(\psi;\mathbf{x},t) \equiv \sum_{n=1}^{N} p_n(\mathbf{x},t) \prod_{\alpha=1}^{m} \delta\left[\psi_\alpha - \langle \phi_\alpha \rangle_n(\mathbf{x},t)\right] \quad (3)$$

where $f_\phi(\psi;\mathbf{x},t)$ is the joint PDF of all scalars (such as concentrations, moments, and so on) appearing in the precipitation model, $p_n(\mathbf{x},t)$ is the probability of mode n, $\langle \phi_\alpha \rangle_n(\mathbf{x},t)$ is the value of scalar α corresponding to mode n, N is the total number of modes, and m is the total number of scalars. By definition, the probabilities p_n sum to unity and the average value of any scalar is defined by integration with respect to ψ. As shown below, for the system under consideration, knowledge of the mixture fraction and a reaction progress variable suffices to predict the reactant concentrations in each environment. Thus, we will let the first scalar be the mixture fraction; $\phi_1(\mathbf{x},t) \equiv \xi(\mathbf{x},t)$.

From Eq. 3, the average value of the mixture fraction is given by

$$\langle \xi \rangle \equiv \sum_{n=1}^{N} p_n \langle \xi \rangle_n, \quad (4)$$

whereas the mixture fraction variance is

$$\langle \xi'^2 \rangle = \langle \xi^2 \rangle - \langle \xi \rangle^2, \quad (5)$$

where $\langle \xi^2 \rangle$ is the second moment of the mixture fraction

$$\langle \xi^2 \rangle \equiv \sum_{n=1}^{N} p_n \langle \xi \rangle_n^2. \quad (6)$$

This approach has been successfully used to model micromixing in precipitation (Piton et al., 2000), and these first results showed that three modes ($N = 3$) are sufficient to work with good accuracy. The 3-mode PDF model can be thought of as the discretization of the reacting system in three environments, where Environments 1 and 2 contain unmixed reactants A and B, respectively, and reaction/particle formation occurs in Environment 3.

The scalar transport equations for the probabilities of modes 1 and 2, and for the weighted mixture fraction in Environment 3 ($s_3 \equiv p_3 \langle \xi \rangle_3$) are (repeated indices imply summation)

$$\frac{\partial p_1}{\partial t} + \frac{\partial}{\partial x_i}\left(\langle u_i \rangle p_1\right) = \frac{\partial}{\partial x_i}\left(\Gamma_t \frac{\partial p_1}{\partial x_i}\right) + \gamma_s p_3 - \gamma p_1 (1 - p_1), \quad (7)$$

$$\frac{\partial p_2}{\partial t} + \frac{\partial}{\partial x_i}\left(\langle u_i \rangle p_2\right) = \frac{\partial}{\partial x_i}\left(\Gamma_t \frac{\partial p_2}{\partial x_i}\right) + \gamma_s p_3 - \gamma p_2 (1 - p_2), \quad (8)$$

$$\frac{\partial s_3}{\partial t}+\frac{\partial}{\partial x_i}\left(\langle u_i\rangle s_3\right)=\frac{\partial}{\partial x_i}\left(\Gamma_t\frac{\partial s_3}{\partial x_i}\right)$$
$$-\gamma_s p_3(\langle\xi\rangle_1+\langle\xi\rangle_2)+\gamma p_1(1-p_1)\langle\xi\rangle_1$$
$$+\gamma p_2(1-p_2)\langle\xi\rangle_2. \quad (9)$$

where $p_3=1-p_1-p_2$, $\langle u_i\rangle$ is the mean velocity in the i^{th} direction, Γ_t is the turbulent diffusivity modeled as

$$\Gamma_t=\frac{C_\mu}{Sc_t}\frac{k^2}{\epsilon}, \quad (10)$$

whereas γ and γ_s are, respectively, the micromixing rate and the spurious dissipation rate. Note that γ_s is required to eliminate spurious scalar dissipation resulting from the finite-mode representation, as will become clear below.

In this work the mixture fraction in Environments 1 and 2 are, respectively, $\langle\xi\rangle_1=1$ and $\langle\xi\rangle_2=0$, and thus the mean mixture fraction is equal to

$$\langle\xi\rangle=p_1+s_3, \quad (11)$$

whereas the variance is given by

$$\langle\xi'^2\rangle=p_1+\frac{s_3^2}{p_3}-\langle\xi\rangle^2. \quad (12)$$

Manipulation of Eq. 11 leads to the transport equation of a conserved passive scalar, and manipulation of Eq. 12 leads to

$$\frac{\partial\langle\xi'^2\rangle}{\partial t}+\frac{\partial}{\partial x_i}\left(\langle u_i\rangle\langle\xi'^2\rangle\right)=\frac{\partial}{\partial x_i}\left(\Gamma_i\frac{\partial\langle\xi'^2\rangle}{\partial x_i}\right)$$
$$+2\Gamma_t\frac{\partial\langle\xi\rangle}{\partial x_i}\frac{\partial\langle\xi\rangle}{\partial x_i}-2\langle\epsilon_\xi\rangle_s-2\langle\epsilon_\xi\rangle \quad (13)$$

where $\langle\epsilon_\xi\rangle_s$ and $\langle\epsilon_\xi\rangle$ are

$$\langle\epsilon_\xi\rangle_s=\Gamma_t p_3\frac{\partial\langle\xi\rangle_3}{\partial x_i}\frac{\partial\langle\xi\rangle_3}{\partial x_i}-\frac{\gamma_s}{2}p_3\left[1+2\langle\xi\rangle_3^2-2\langle\xi\rangle_3\right], \quad (14)$$

$$\langle\epsilon_\xi\rangle=\frac{\gamma}{2}\left[p_1(1-p_1)(1-\langle\xi\rangle_3)^2+p_2(1-p_2)\langle\xi\rangle_3^2\right], \quad (15)$$

and $\langle\xi\rangle_3=s_3/p_3$ is the mixture fraction in Environment 3.

Except for the spurious scalar dissipation rate $\langle\epsilon_\xi\rangle_s$, Eq. 13 is identical to the scalar variance transport equation for a conserved passive scalar. However, from Eq. 14 it can be seen that $\langle\epsilon_\xi\rangle_s$ can be eliminated by setting γ_s as follows

$$\gamma_s=\frac{2\Gamma_t}{1-2\langle\xi\rangle_3(1-\langle\xi\rangle_3)}\frac{\partial\langle\xi\rangle_3}{\partial x_i}\frac{\partial\langle\xi\rangle_3}{\partial x_i}. \quad (16)$$

The term $\langle\epsilon_\xi\rangle$ is the scalar dissipation rate due to micromixing. Writing a transport equation for the scalar dissipation rate (Fox 1995, 1997, 1999), it is possible to see that for a fully-developed scalar spectrum the scalar mixing rate is related to the turbulent frequency (ϵ/k) by

$$\frac{2\langle\epsilon_\xi\rangle}{\langle\xi'^2\rangle}=C_\phi\frac{\epsilon}{k} \quad (17)$$

where $C_\phi\approx 1-2$. Using Eqs. 17 and 15, an expression for γ is found

$$\gamma=C_\phi\frac{\epsilon}{k}\frac{\langle\xi'^2\rangle}{\left[p_1(1-p_1)(1-\langle\xi\rangle_3)^2+p_2(1-p_2)\langle\xi\rangle_3^2\right]}. \quad (18)$$

Although this expression could be used to define γ at any point in the flow, we will make use of a simpler expression in which the last term was included in the constant C_ϕ, resulting in

$$\gamma=C_\phi\frac{\epsilon}{k}. \quad (19)$$

In order to take into account this correction, we use a value of $C_\phi=0.5$. However, it is found that the simulation results are relatively insensitive to the choice of the value of C_ϕ.

The numerical values of the constants used in the simulations are reported in Table 1. The model equations are added to FLUENT as user-defined scalars. For every user-defined scalar, a transport equation of the form

$$\rho\frac{\partial\phi_k}{\partial t}+\frac{\partial}{\partial x_i}\left(\rho\langle u_i\rangle\phi_k-\rho\Gamma_k\frac{\partial\phi_k}{\partial x_i}\right)=S_{\phi k} \quad (20)$$

is solved, where ϕ_k is the k^{th} scalars, ρ is the fluid density, and Γ_k and S_{ϕ_k} are the diffusivity and the source term for the k^{th} scalar, respectively.

In this work the diffusivity Γ_k has been set equal to the turbulent diffusivity (Γ_t) for all scalars. Note that the source term must be consistent with the dimensions of the other

Table 1. Model Constants used in the Simulations

C_μ	0.09
Sc_t	0.7
C_ϕ	0.5

terms in Eq. 20. For this reason, the source terms appearing in Eqs. 7–9 are multiplied by the fluid density. For example, the source term for the first scalar (p_1) is given by

$$S_{p_1} = \rho\left[\gamma_s p_3 - \gamma p_1(1-p_1)\right]. \tag{21}$$

Mixture fraction approach

The mixing between two feedstreams in a reactor can be described using the mixture fraction approach (Fox, 1996). For a simple reaction (that is, $A + B \rightarrow C$) in the case of two nonpremixed feeds, the mixture fraction is a conserved scalar defined as follows

$$\xi = \frac{c_A - c_B + c_{Bo}}{c_{Ao} + c_{Bo}} \tag{22}$$

where c_{Ao} and c_{Bo} are the inlet concentrations of the two reactants in their separate feed streams. From Eq. 22, it is clear that the mixture fraction is equal to 1 in one feedstream ($c_A = c_{Ao}$; $c_B = 0$) and 0 in the other ($c_A = 0$; $c_B = c_{Bo}$). In the case of a nonreacting system, the relationships between the mixture fraction and the reactant concentrations are

$$\frac{c_A^0}{c_{Ao}} = \xi, \ \frac{c_B^0}{c_{Bo}} = 1 - \xi \tag{23}$$

where c_A^0 and c_B^0 are the reactant concentrations in the case of mixing without reaction.

In the case of an instantaneous reaction, the two reactants cannot coexist at the same point, and thus the mixture fraction is related to the reactant concentrations as follows

$$\frac{c_A^\infty}{c_{Ao}} = \begin{cases} 0 & \text{for} \quad \xi < \xi_s \\ \dfrac{\xi - \xi_s}{1 - \xi_s} & \text{for} \quad \xi \geq \xi_s \end{cases},$$

$$\frac{c_B^\infty}{c_{Bo}} = \begin{cases} 1 - \dfrac{\xi}{\xi_s} & \text{for} \quad \xi < \xi_s \\ 0 & \text{for} \quad \xi \geq \xi_s \end{cases} \tag{24}$$

where

$$\xi_s = \frac{c_{Bo}}{c_{Ao} + c_{Bo}}. \tag{25}$$

In the case of a finite-rate chemical reaction, the source term can be closed using a reaction progress variable. Using this approach, the relationships between concentrations, the mixture fraction, and the reaction progress variable (Y) are

$$\frac{c_A}{c_{Ao}} = \xi - \xi_s Y, \qquad \frac{c_B}{c_{Bo}} = (1-\xi) - (1-\xi_s)Y. \tag{26}$$

Note that since it is proportional to the amount of reaction product, Y is null in the feedstreams where no reaction occurs (that is, in Environments 1 and 2). Thus, in order to close the problem, a transport equation for the mean reaction progress variable $\langle Y \rangle = p_3 \langle Y \rangle_3$ must be added

$$\frac{\partial \langle Y \rangle}{\partial t} + \frac{\partial}{\partial x_i}\left(\langle u_i \rangle \langle Y \rangle\right) = \frac{\partial}{\partial x_i}\left(\Gamma_t \frac{\partial \langle Y \rangle}{\partial x_i}\right) + \frac{p_3 S\left(\langle c_A \rangle_3, \langle c_B \rangle_3\right)}{\xi_s c_{Ao}} \tag{27}$$

where $S(\langle c_A \rangle_3, \langle c_B \rangle_3)$ is the source term for the chemical reaction, and $\langle c_A \rangle_3$ and $\langle c_B \rangle_3$ are defined in terms of s_3, p_3 and $\langle Y \rangle$ by

$$\frac{\langle c_A \rangle_3}{c_{Ao}} = \frac{s_3 - \xi_s \langle Y \rangle}{p_3}, \qquad \frac{\langle c_B \rangle_3}{c_{Bo}} = \frac{p_3 - s_3 - (1-\xi_s)\langle Y \rangle}{p_3}. \tag{28}$$

Micromixing will influence the predictions of the model in regions where $p_3 < 1$, whereas in perfectly micromixed regions $p_3 = 1$. The local reactant concentration will thus be greater than the mean concentration whenever $p_3 < 1$, resulting in increased rates of nucleation and growth.

The reactive system can thus be studied using Eqs. 7 and 8 to describe the spatial and temporal evolution of the volume fractions of Environments 1 and 2, using Eq. 9 to describe the evolution of the mixture fraction in Environment 3, and using Eq. 27 to account for the chemical reaction in Environment 3. Equation 28 is used to relate the reactant concentrations to the mixture fraction and the mean reaction progress variable. The problem will thus be closed once a functional form has been specified for $S(c_A, c_B)$.

Moment method approach

The CSD can be described by a population balance (Randolph and Larson, 1988). This equation is a continuity statement expressed in terms of the particle number density $n(L; \mathbf{x}, t)$, that is, function of time (t), position ($\mathbf{x}$), and particle dimension (L). This function multiplied by an infinitesimal increment in the particle dimension [that is, $n(L; \mathbf{x}, t)dL$] represents the number density of particles with dimensions between L and $L + dL$. In order to obtain a simpler expression, the population balance can be expressed in terms of the moments of the particle number density function. Note that since nucleation and growth occur only in Environment 3, the population balance need only be applied to one environment. With this approach, the governing equations for the CSD moments are (Rivera and Randolph, 1978)

$$\frac{\partial m_0}{\partial t} + \frac{\partial}{\partial x_i}\left(\langle u_i \rangle m_0\right) = \frac{\partial}{\partial x_i}\left(\Gamma_t \frac{\partial m_0}{\partial x_i}\right) + B\left(\langle c_A \rangle_3, \langle c_B \rangle_3\right) p_3, \tag{29}$$

$$\frac{\partial m_1}{\partial t} + \frac{\partial}{\partial x_i}\left(\langle u_i \rangle m_1\right) = \frac{\partial}{\partial x_i}\left(\Gamma_t \frac{\partial m_1}{\partial x_i}\right) + G\left(\langle c_A \rangle_3, \langle c_B \rangle_3\right) m_0, \tag{30}$$

$$\frac{\partial m_2}{\partial t}+\frac{\partial}{\partial x_i}\left(\langle u_i\rangle m_2\right)=\frac{\partial}{\partial x_i}\left(\Gamma_t\frac{\partial m_2}{\partial x_i}\right)+2G\left(\langle c_A\rangle_3,\langle c_B\rangle_3\right)m_1, \tag{31}$$

$$\frac{\partial m_3}{\partial t}+\frac{\partial}{\partial x_i}\left(\langle u_i\rangle m_3\right)=\frac{\partial}{\partial x_i}\left(\Gamma_t\frac{\partial m_3}{\partial x_i}\right)+3G\left(\langle c_A\rangle_3,\langle c_B\rangle_3\right)m_2, \tag{32}$$

$$\frac{\partial m_4}{\partial t}+\frac{\partial}{\partial x_i}\left(\langle u_i\rangle m_4\right)=\frac{\partial}{\partial x_i}\left(\Gamma_t\frac{\partial m_4}{\partial x_i}\right)+4G\left(\langle c_A\rangle_3,\langle c_B\rangle_3\right)m_3, \tag{33}$$

where B is the nucleation rate, G is the growth rate, and m_j is the mean value of the jth moment of the particle number density function (that is, $m_j=p_3\langle m_j\rangle_3$).

The first five moments are computed only in Environment 3 where the reaction occurs. Using this approach, the mean crystal size can be written as follows

$$d_{43}=\frac{m_4}{m_3}, \tag{34}$$

and the solid concentration is given by

$$c_C=\frac{\rho k_v}{M}m_3, \tag{35}$$

where ρ is the crystal density, k_v is the volume shape factor, and M is the molecular weight of the crystal.

The chemical source term appearing in Eq. 27 can be expressed in terms of m_2 and G as follows

$$p_3S\left(\langle c_A\rangle_3,\langle c_B\rangle_3\right)=\frac{\rho k_v}{M}3G\left(\langle c_A\rangle_3,\langle c_B\rangle_3\right)m_2. \tag{36}$$

The model equations can thus be closed by supplying expressions for the nucleation and growth rates for barium sulfate precipitation.

Precipitation kinetics and shape factors

Barium sulfate precipitation from aqueous solution has been widely used to validate micromixing models and to study the influence of mixing. In the literature several kinetic expressions have been proposed. In this study, we have used the following kinetic scheme:

- Baldyga and coworkers (Baldyga et al., 1995) used a power law for the nucleation rate:

$$B(c_A,c_B)=\begin{cases}2.83\times10^{10}\Delta c^{1.775}\ \left(1/\mathrm{m}^3\cdot\mathrm{s}\right) & \text{for } \Delta c\le 10\ \mathrm{mol/m}^3\ \text{(heterogeneous)}\\ 2.53\times10^{-3}\Delta c^{15}\ \left(1/\mathrm{m}^3\cdot\mathrm{s}\right) & \text{for } \Delta c>10\ \mathrm{mol/m}^3\ \text{(homogeneous)}\end{cases} \tag{37}$$

where $\Delta c=\sqrt{c_Ac_B}-\sqrt{k_s}$, and k_s is the solubility product of barium sulfate (at room temperature $k_s=1.14\times10^{-4}$ $\mathrm{mol}^2/\mathrm{m}^6$).

- Starting from the results obtained by Nielsen (1969), Aoun et al. (1996) found an expression for the growth rate which takes into account the effect of nonstoichiometric conditions

$$G(c_A,c_B)=k_G\left(c_A-\sqrt{k_s}\right)^{1.15}\left(c_B-\sqrt{k_s}\right)^{0.95}\ (m/s) \tag{38}$$

where

$$k_G=\begin{cases}1.05\times10^{-5}10^{-1.57/R_o} & \text{for} \quad R_o>1\\ 2.73\times10^{-5}R_o^{-1.99R_o} & \text{for} \quad R_o\le 1\end{cases} \tag{39}$$

and $R_o=c_A/c_B$.The volume shape factor used in our calculations were taken from Pagliolico et al. (1999). These authors, using SEM images of individual crystals, found that the value given from the instrument (Laser Coulter particle sizer) is intermediate between the values of the length and the width of the crystals, but generally closer to the latter. Depending on the observed morphologies, different characteristic dimensions have been used and the resulting shape factor was used to evaluate its influence on the final mean crystal size predicted by a simple model (Marchisio et al., 2000). Based on these results, a "best-fit" value for the volume shape factor ($k_v=0.06$) was derived.

Results and Discussion

Time-dependent simulations of the semi-batch precipitation reaction were carried out in an axial section of the reactor. Three different unstructured grids with different resolution near the injection zone were created using Gambit, and the solution was shown to be grid independent. The turbulent flow field was solved first, until a steady-state solution was achieved. Using this flow field, a total of nine transport equations (Eqs. 7–9, 27, 29–33) were solved as user-defined scalars in FLUENT.

The initial conditions for the computational domain inside the reactor are as follows

$$p_1=0,\quad p_2=1,\quad s_3=\langle Y\rangle=m_0=m_1=m_2=m_3=m_4=0, \tag{40}$$

whereas at the inlet point

$$p_1=1,\quad p_2=0,\quad s_3=\langle Y\rangle=m_0=m_1=m_2=m_3=m_4=0. \tag{41}$$

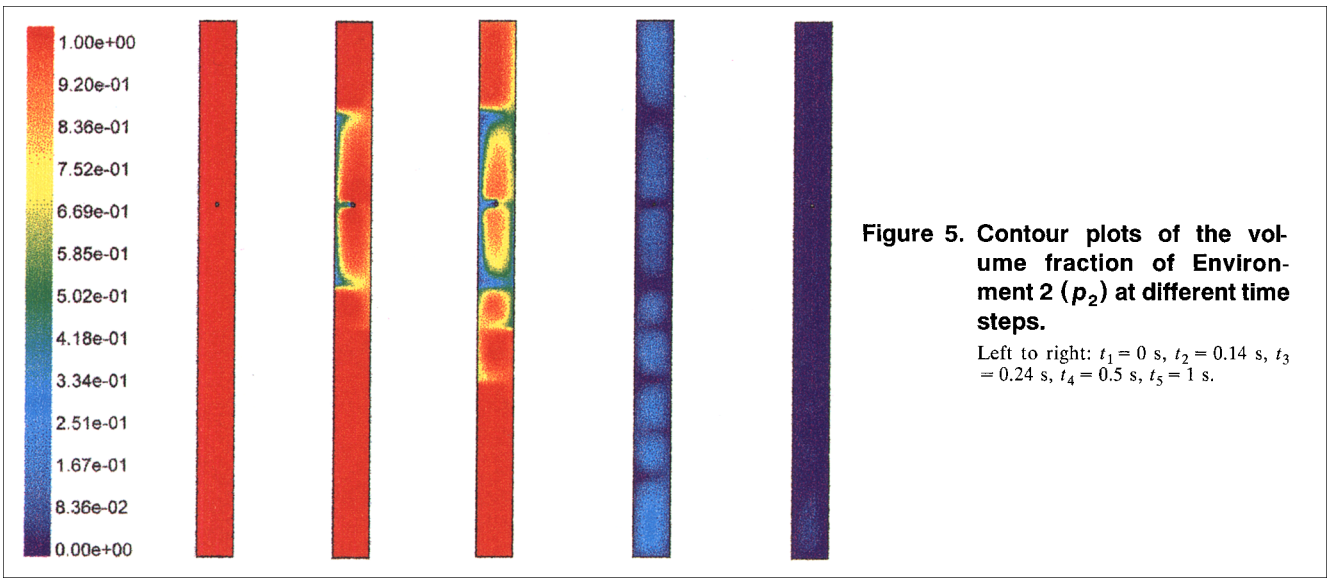

Figure 5. Contour plots of the volume fraction of Environment 2 (p_2) at different time steps.

Left to right: $t_1 = 0$ s, $t_2 = 0.14$ s, $t_3 = 0.24$ s, $t_4 = 0.5$ s, $t_5 = 1$ s.

With these initial conditions, sodium sulfate is the reactant in Environment 2, whereas barium chloride is the reactant in Environment 1. During injection, barium chloride enters the reactor, and, successively, due to micromixing, moves to Environment 3. In the same way, sodium sulfate moves to Environment 3 where the reaction takes place.

The time-dependent simulations were carried out with a variable time step. Generally, when the concentrations of the reactants are locally high, the problem becomes stiff, and thus the time step has to be sufficiently small to avoid floating point errors. For low values of the initial nominal supersaturation ratio (S_o) and high values of the volume ratio (f), the time step has been kept constant and equal to 1 s, whereas at high values of the initial nominal supersaturation ratio and low values of the volume ratio, the time step has been initially fixed to 10^{-4} s. As soon as the simulation had successfully completed one time iteration, the time step was increased to 0.1 s. We have to highlight that because the exponent in Eq. 37 for homogeneous nucleation is very large (Δc^{15}), all calculations were carried out in double precision.

Mixing properties

In Figure 5 contour plots of the volume fraction of Environment 2 at different time steps are reported. At the beginning of the simulation, the reactor is occupied by Environment 2 except at the injection period. As soon as Environment 1 enters into the reactor, Environment 2 starts to disappear due to mixing. After approximately one second, Environment 3 has completely taken the place of Environment 2, except near the injection zone, where the volume fraction of Environment 3 will not be equal to one until the injection is finished.

The volume-averaged profiles of the volume fractions of Environments 1 and 2 for different injection velocities are reported in Figures 6 and 7, respectively. From the figures, it is clear that the injection velocity has little effect on the temporal evolution of Environment 2, but has a strong effect on the temporal evolution of Environment 1. In fact, Figure 6 shows that different injection velocities imply different injection times, and, moreover, the value of the volume fraction of Environment 1 during the injection increases with decreasing injection velocity. Note, however, that even at high injection velocities the volume fraction of Environment 1 remains relatively small.

From these observations, we can draw the following conclusions concerning mixing in this reactor. Within 1 s, (see Figures 5 and 6), large-scale gradients due to the initial conditions are eliminated. The reactor then operates in a steady-state regime until the injection is finished (see Figure 6). During this period, the largest gradients (and, hence, mi-

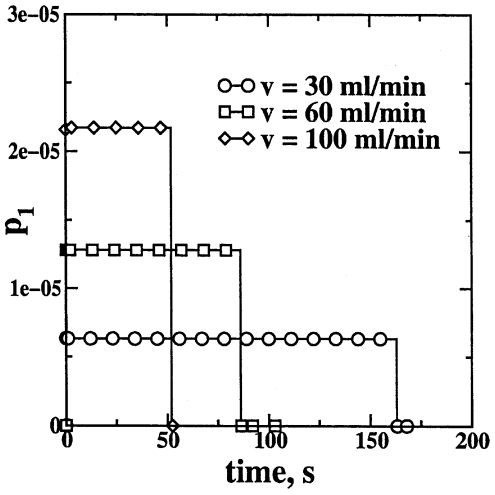

Figure 6. Volume-averaged volume fraction of Environment 1 for three different injection velocities ($N = 500$ rpm).

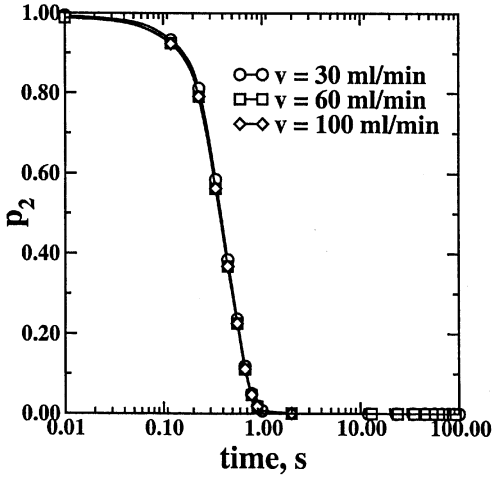

Figure 7. Volume-averaged volume fraction of Environment 2 for three different injection velocities ($N = 500$ rpm).

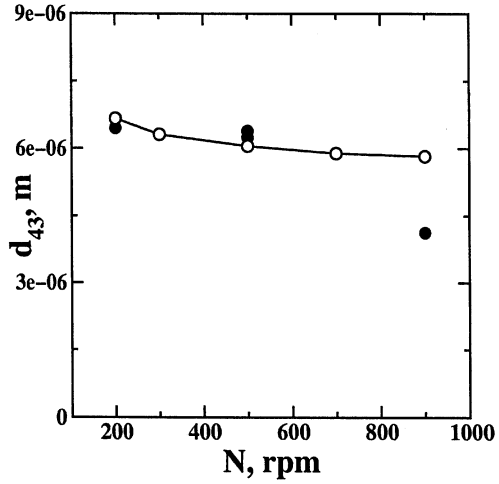

Figure 8. Final mean crystal size vs. speed of the internal cylinder ($v = 60$ mL/min, $f = 0.1$, $\log(S_o) = 4$).

Open symbols: CFD prediction. Filled symbols: experimental data.

cromixing) are concentrated in a small volume surrounding the injection period. At the end of the injection period, all gradients in mixture fraction are quickly eliminated and the system behaves like a perfectly mixed batch reactor. Thus, despite the fact that the micromixing parameter C_ϕ was chosen smaller than the value for fully-developed turbulence, the effect of micromixing on the overall process was found to be very small.

Effect of operating conditions

The effect of the operating conditions on supersaturation (S), total particle number density (m_0), and mean crystal size (d_{43}) has been studied. The reported values of these variables are volume-averaged values over all the reactor. In the case of precipitation, the interpretation of the results is often difficult and controversial because of the many phenomena involved [that is, mixing at various scales (macro-, meso- and micro-mixing), nucleation and growth]. Moreover, the effect of varying a single parameter can be different depending on the controlling process. For example, an increase in the intensity of mixing can reduce the volume-average intensity of segregation of the reactant favoring nucleation, or reduce the local peak of supersaturation disfavoring nucleation.

Effect of Rotation Speed. The effect of the rotational speed of the impeller on the crystal size has been analyzed by several authors, and different results and conclusions have been found. Kim and Tarbell (1996) found a maximum of the mean crystal size vs. the stirrer speed, while Phillips et al. (1999) and Fitchett and Tarbell (1990) found a monotonic increase. Differently from what is observed in the continuous apparatus (Barresi et al., 1999), in the semi-batch Taylor-Couette reactor both the model and the experimental data show a decrease of the mean crystal size when plotted against the rotational speed of the internal cylinder (Figure 8). This effect could be caused by enhanced macromixing, which reduces the degree for segregation of the reactants and favors nucleation. The final effect is to produce a slightly higher number of particles, but with a lower dimension.

In Figure 9 a plot of the solids concentration against the speed of the internal cylinder is reported. The figure shows that the rotational speed does not significantly affect the final solid concentration. In fact, given that the experiments were sufficiently long for the reactants to completely react, this result was included only to show that the overall mass balance was satisfied. The same behavior for the final solids concentration has been found for all other parameters, except for the initial nominal supersaturation, as will be explained below.

Effect of Injection Velocity. In Figure 10 the volume-averaged supersaturation profiles are reported for three injection velocities. The observed discontinuity in the derivative of the

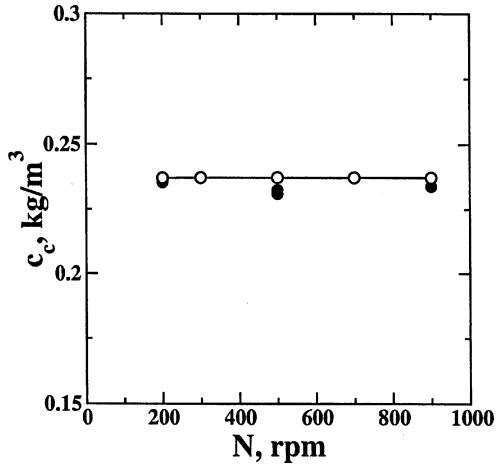

Figure 9. Final solid concentration vs. speed of the internal cylinder ($v = 60$ mL/min, $f = 0.1$, $\log(S_o) = 4$).

Open symbols: CFD prediction. Filled symbols: experimental data.

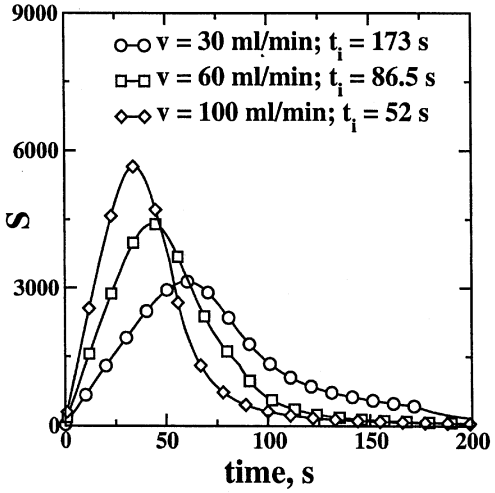

Figure 10. Volume-averaged supersaturation vs. time for three injection velocities ($N = 500$ rpm, $f = 0.1$, $\log(S_o) = 4$).

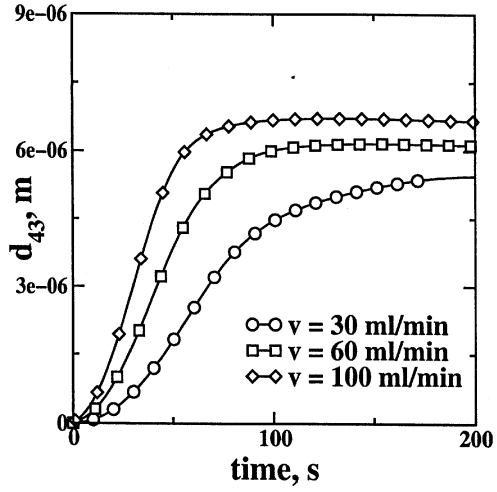

Figure 12. Volume-averaged mean crystal size vs. time for three injection velocities ($N = 500$ rpm, $f = 0.1$, $\log(S_o) = 4$).

profile occurs at the end of the injection period. From the figure is clear that increasing the injection velocity results in a higher peak of supersaturation. However, the supersaturation subsequently decreases more rapidly due to crystal growth. Overall, the supersaturation is kept at a higher time-averaged value with low injection velocity and this effect causes the formation of a higher number of particles (Figure 11) with a lower dimension (Figure 12) under these conditions. A comparison with the experimental data for the volume-averaged mean crystal size at the end of the reaction is reported in Figure 13, and good agreement has been found.

Effect of Initial Nominal Supersaturation. The effect of the initial nominal supersaturation ratio (S_o) has been studied for values between 10^4 and 10^6. The profiles of the volume-averaged supersaturation for three different initial nominal supersaturation ratios are reported in Figure 14. From the figure, it is clear that by increasing this ratio, the peak of the supersaturation is also increased. It has to be highlighted that for the highest initial supersaturation ratio after the peak, the reaction starts to remove the reactants, but, after a while, the injection of fresh reactants makes the profile rise again. This is caused by the large number of particles, created by the high supersaturation, that grow rapidly due to the enhanced growth rate, and remove the reactants. After this period, the fresh reactants are almost completely segregated in different vortices in the bottom and in the top of the reactor (see Figure 15), and it is necessary to wait for the end of the injection in order to have a further decrease of the concentration.

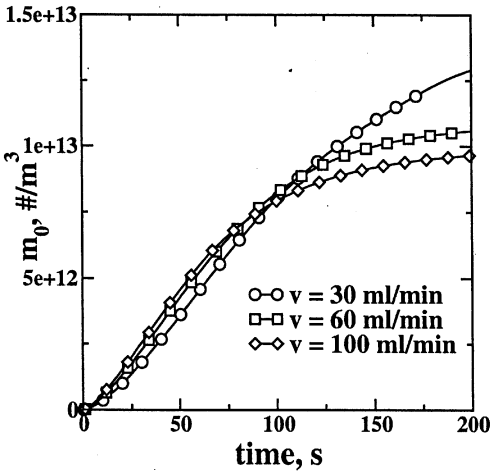

Figure 11. Volume-average total particle number density vs. time for three injection velocities ($N = 500$ rpm, $f = 0.1$, $\log(S_o) = 4$).

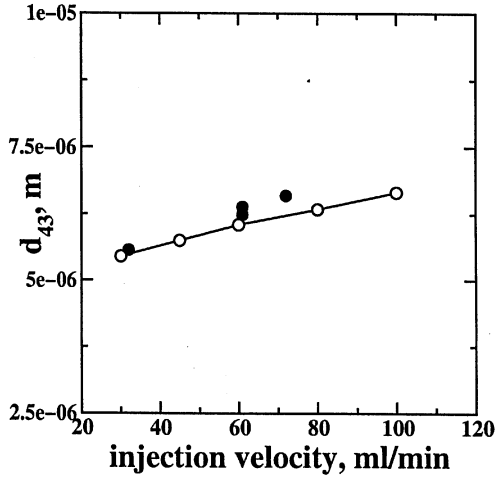

Figure 13. Final mean crystal size vs. injection velocity ($N = 500$ rpm, $f = 0.1$, $\log(S_o) = 4$).

Open symbols: CFD prediction. Filled symbols: experimental data.

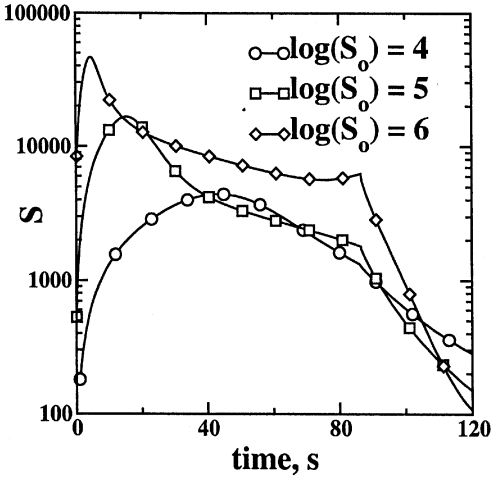

Figure 14. Volume-averaged supersaturation profiles vs. time for three initial nominal supersaturation ratios ($v = 60$ mL/min, $f = 0.1$, $N = 500$ rpm).

We saw earlier that during the injection period the reactor operates in a steady-state regime where the mixture fraction is slightly larger at the top of the reactor than at the bottom.

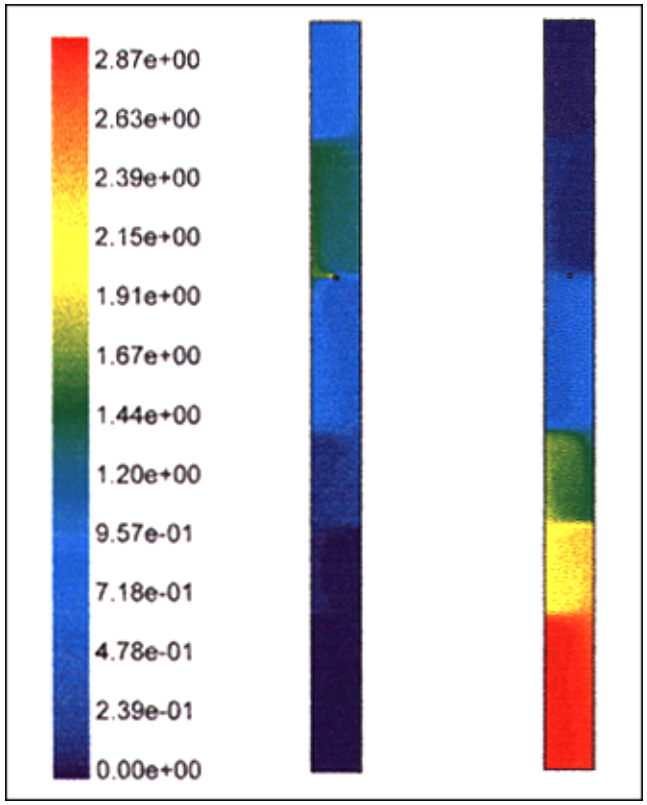

Figure 15. Contour plots of reactant concentrations in Environment 3 at the end of the injection period ($v = 60$ mL/min, $f = 0.1$, $N = 500$ rpm, $t =$ 86.5 s).

Left: $\langle c_A \rangle_3$, mol/m^3, right: $\langle c_B \rangle_3$, mol/m^3.

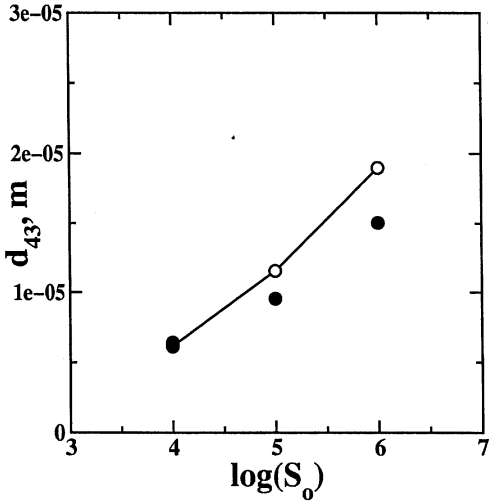

Figure 16. Experimental data for the final mean crystal size vs. the initial nominal supersaturation ratio ($v = 60$ mL/min, $f = 0.1$, $N = 500$ rpm).

Open symbols: CFD predictions. Filled symbols: experimental data.

Due to the nonlinear nature of the nucleation rate, at high supersaturation, this small macroscale gradient is amplified in the reactant concentrations, leading to the macroscale segregation seen in Figure 15. Such large-scale, reaction-induced segregation could not be predicted without resorting to CFD.

The comparison with the experimental data is reported in Figure 16 for different initial nominal supersaturation ratios. Under these conditions, an increase in S_o accelerates crystal growth more than nucleation, because the heterogeneous nucleation order (1.775) is smaller than the overall growth order (2.1). For higher S_o, the homogeneous nucleation order (Eq. 15) becomes very high and a further increase would cause more crystals of smaller size. From Figure 16, it is possible to see that both model and experiments show an increase in the mean crystal size with increasing S_o. However, the model overpredicts the rate of increase, because of the strong segregation in the system due to the vortices, that causes poor macromixing. This result, once again, shows the importance of an accurate knowledge of the flow field, in order to predict its effect on the final CSD.

Effect of Reactant Volume Ratio. The effect of the reactant volume ratio has been studied for two different values of the initial nominal supersaturation ratio [$\log(S_o) = 4$ and 6]. The results are reported in Figure 17 and the model predictions for $\log(S_o) = 4$ are compared with experimental data. To be consistent with our earlier terminology, the volume ratio (f) is the volume average of the mean mixture fraction $\langle \xi \rangle$ at the end of the injection period; in fact, it represents the final volume fraction of fluid injected into the reactor. In order to maintain a 1:1 stoichiometric ratio, decreasing f results in a higher concentration of the reactant over a shorter injection time at the same flow rate. This results in a significant increase of the local supersaturation near the injection point. Depending on the initial nominal supersaturation, this local increase can favor nucleation or growth.

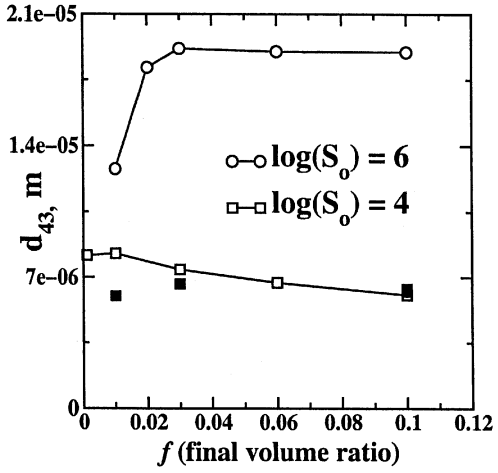

Figure 17. Final mean crystal size vs. mean mixture fraction for two different initial supersaturation ratios ($N = 500$ rpm, $v = 60$ mL/min).

Open symbols: CFD predictions, filled symbols: experimental data.

At low values of the initial nominal supersaturation ratio [$\log(S_o) = 4$], the local value of the supersaturation is not high enough to induce homogeneous nucleation, and this results in a smaller number of crystals with higher dimension. However, when the initial nominal supersaturation ratio is increased to 10^6, the local value of the supersaturation leads to homogeneous nucleation and a higher number of particles with lower dimension are produced. Furthermore, a decrease in the mean crystal size is observed in the simulations for volume ratios lower than 0.01 for $\log(S_o) = 4$, and 0.03 for $\log(S_o) = 6$. In the first case, only when the volume ratio is lower than 0.01 is the local value of the supersaturation high enough to favor nucleation over growth. In the second case, this condition is satisfied for volume ratios less than 0.1. The fact that the mean crystal size starts to decrease with a decreasing volume ratio at lower values of this parameter is due to the segregation of the fresh reactants as explained above (Figure 15). Only when the volume ratio is small enough to have a short injection time will the introduction of the reactant be faster than the growth process, so that during the injection the high local supersaturation favors nucleation.

Conclusions

A finite-mode PDF model coupled with a CFD code (FLUENT) has been used to model precipitation of barium sulfate in a semibatch Taylor-Couette reactor. The CSD has been calculated in terms of the first five moments of the CSD and the model has been validated with experimental data. The effects of various operating conditions (speed of the internal cylinder, injection velocity, initial nominal supersaturation, reactants volume ratio) have been investigated. The results show that the precipitation reaction is strongly influenced by the local value of supersaturation at high reactant concentrations. Mixing at various scales has been found to be the controlling phenomenon and in particular the vortical structure of the flow in the Taylor-Couette reactor favors the role of macromixing. The use of time-dependent CFD has been shown to be a feasible modeling approach for predicting the behavior of the reactor. Although the flow field has been validated only through tracer experiments, and no direct information on the turbulent flow field is available for model validation, the overall agreement with experimental data is satisfactory. Nevertheless, a detailed investigation of the flow field (such as using LDV or PIV) will be required in order to completely verify the effect of turbulence parameters on the degree of mixing at various scales in the reactor.

Acknowledgments

The research has been partially supported by an Italian National research project (MURST 40%-Multiphase reactors: hydrodynamics analysis and solid-liquid analysis) and a U.S. NSF grant (CTS-9996264).

Literature Cited

Aoun, M., E. Plasari, R. David, and J. Villermaux, "Are Barium Sulphate Kinetics Sufficiently Known for Testing Precipitation Reactor Models?," *Chem. Eng. Sci.*, **51**, 2449 (1996).

Baldyga, J., and W. Orciuch, "Closure Problem for Precipitation," *Chem. Eng. Res. Des.*, **75A**, 160 (1997).

Baldyga, J., and W. Orciuch, "Closure Method for Precipitation in Inhomogeneous Turbulence," *Proc. of 14th Symp. on Ind. Crystallization*, paper 86, Rugby, UK, 1069 (Sept. 12-16, 1999).

Baldyga, J., R. Pohorecki, W. Podgorska, and B. Marcant, "Micromixing Effects in Semibatch Precipitation," *Proc. Symp. on Ind. Crystallization*, A. Mersmann, ed., Garmisch-Partenkirchen, RFG, 175 (1990).

Baldyga, J., W. Podgorska, and R. Pohorecky, "Mixing Precipitation Model with Application to Double Feed Semibatch Precipitation," *Chem. Eng. Sci.*, **50**, 1281 (1995).

Barresi, A. A., D. Marchisio, and G. Baldi, "On the Role of Micro- and Mesomixing in a Continuous Couette-Type Precipitator," *Chem. Eng. Sci.*, **54**, 2339 (1999).

Fitchett, D. E., and J. M. Tarbell, "Effect of Mixing on the Precipitation of Barium Sulphate in an MSMPR Reactor," *AIChE J.*, **36**, 511 (1990).

Fluent Inc., "Fluent 5 User's Guide," Fluent Inc., Lebanon, NH (1990).

Fox, R. O., "The Spectral Relaxation Model of the Scalar Dissipation Rate in Homogeneous Turbulence," *Phys. Fluid*, **7**, 1082 (1995).

Fox, R. O., "Computational Methods for Turbulent Reacting Flows in the Chemical Process Industry," *Revue de l'Institute Francais du Petrole*, **51**, 215 (1996).

Fox, R. O., "The Lagrangian Spectral Relaxation Model of the Scalar Dissipation Rate in Homogeneous Turbulence," *Phys. Fluid*, **9**, 2364 (1997).

Fox, R. O., "On the Relationship Between Lagrangian Micromixing Models and Computational Fluid Dynamics," *Chem. Eng. Proc.*, **37**, 521 (1998).

Fox, R. O., "The Lagrangian Spectral Relaxation Model for Differential Diffusion in Homogeneous Turbulence," *Phys. Fluid*, **11**, 1550 (1999).

Garside, J., and N. S. Tavare, "Mixing, Reaction and Precipitation: Limits of Micromixing in an MSMPR Crystallizer," *Chem. Eng. Sci.*, **40**, 1485 (1985).

Kim, W. S., and J. M. Tarbell, "Micromixing Effects on Barium Sulphate Precipitation in a MSMPR Reactor," *Chem. Eng. Comm.*, **146**, 33 (1996).

Marchisio, D., A. A. Barresi, and G. Baldi, "Influence of the Hydrodynamics on the Solid Characteristics in a Couette Type Precipitator," *Proc. of 6th Int. Conf. on Multiphase Flow in Ind. Plants,* Milan, Italy, 335 (Sept. 24-25, 1998).

Marchisio, D. L., A. A. Barresi, G. Baldi, and R. O. Fox, "Comparison of Different Modeling Approaches to Turbulent Precipitation," *Proc. of 10th European Conf. on Mixing,* H. E. A. Van den Akker, ed., Delft, The Netherlands, 77 (July 2–5, 2000).

Nielsen, A. E., "Nucleation and Growth of Crystal at High Supersaturation," *Kristall Technik*, **4**, 17 (1969).

Pagliolico, S., D. Marchisio, and A. A. Barresi, "Influence of Operating Conditions on $BaSO_4$ Crystal Size and Morphology in a Continuous Couette Precipitator," *J. Therm. Anal. Cal.*, **56**, 1423 (1999).

Phillips, R., S. Rohani, and J. Baldyga, "Micromixing in a Single-Feed Semi-Batch Precipitation Process," *AIChE J.*, **45**, 82 (1999).

Pipino, M., A. A. Barresi, and R. O. Fox, "A PDF Approach to the Description of Homogeneous Nucleation," *Proc. of 4th Int. Conf. on Multiphase Flow in Ind. Plants,* Ancona, Italy, 248 (Oct. 6-7, 1995).

Piton, D., R. O. Fox, and B. Marcant, "Simulation of Fine Particle Formation by Precipitation Using Computational Fluid Dynamics," *Can. J. Chem. Eng.*, **78**, 983 (2000).

Pohorecky, R., and J. Baldyga, "The Effect of Micromixing on the Course of Precipitation in an Unpremixed Feed Continuous Tank Crystallizer," *Proc. of 5th Eur. Conf. on Mixing* (BHRA), Wurzburg, West Germany, 105 (1985).

Pohorecky, R., and J. Baldyga, "The Effect of Micromixing and the Manner of Reactor Feeding on Precipitation in Stirrer Tank Reactors," *Chem. Eng. Sci.*, **43**, 1949 (1988).

Randolph, A. D., and M. A. Larson, *Theory of Particulate Processes*, 2nd ed., Academic Press, San Diego (1988).

Rivera, T., and A. D. Randolph, "A Model for the Precipitation of Pentaerythritol Tetranitrate (PETN)," *Ind. Eng. Process Des. Dev.*, **17**, 183 (1978).

Smith, G. P., and A. A. Townsend, "Turbulent Couette Flow Between Concentric Cylinders at Large Taylor Numbers," *J. Fluid Mech.*, **123**, 187 (1982).

Taylor, G. I., "Stability of a Viscous Liquid Contained Between Two Rotating Cylinders," *Phil. Trans. Roy. Soc. A*, **223**, 289 (1923).

Valerio, S., M. Vanni, A. A. Barresi, and G. Baldi, "Engineering Modeling of Turbulent Flows in Chemical Engineering Applications," *Trends Chem. Eng.*, **5**, 1 (1998).

Wei, H., and J. Garside, "Application of CFD Modelling to Precipitation Systems," *Chem. Eng. Res. Des.*, **75a**, 219 (1997).

Manuscript received Mar. 13, 2000, and revision received Aug. 14, 2000.